ACS APPLIED POLYMER MATERIALS

pubs.acs.org/acsapm

Article

# Characterization and Polymerization Kinetics of Triazine-Based Benzoxazine Monomers: Effects of Pyridine and Bromine Interactions

Yang-Chin Kao,[‖] Mohamed Gamal Mohamed,[‖] Pin-Han Chen, Alaa Ali Thabet, Ahmed A. K. Mohammed, and Shiao-Wei Kuo*

Cite This: *ACS Appl. Polym. Mater.* 2025, 7, 10212−10223

Read Online

ACCESS | Metrics & More | Article Recommendations | Supporting Information

**ABSTRACT:** In this work, we report the synthesis and comprehensive characterizations of two series of triazine-based benzoxazine monomers derived from trifunctionalized aniline (TA-TPh-3$NH_2$) and aminopyridine (TA-TPy-3$NH_2$) precursors. The benzoxazine monomers, both with and without bromine substitution, were prepared through sequential Schiff base formation, reduction, and Mannich condensation reactions. Structural elucidation was achieved via Fourier transform infrared spectroscopy (FTIR), thermogravimetric analysis (TGA), differential scanning calorimetry (DSC), and nuclear magnetic resonance (NMR) spectroscopy. Density functional theory (DFT) calculations, reduced density gradient (RDG) analysis, and molecular electrostatic potential (MESP) mapping were performed to probe the electronic structures, noncovalent interactions, and hydrogen bonding influences in these systems. The incorporation of bromine was found to slightly modify the HOMO−LUMO energy gaps, reduce negative electrostatic potential values, and alter polymerization kinetics, as evidenced by dynamic DSC measurements and activation energy ($E_a$) determinations using the Kissinger and Ozawa methods. Overall, our results provide deep insights into how subtle changes in molecular structure, especially bromine substitution and the nature of the heterocycle, influence the thermal and chemical properties of these advanced benzoxazine monomers.

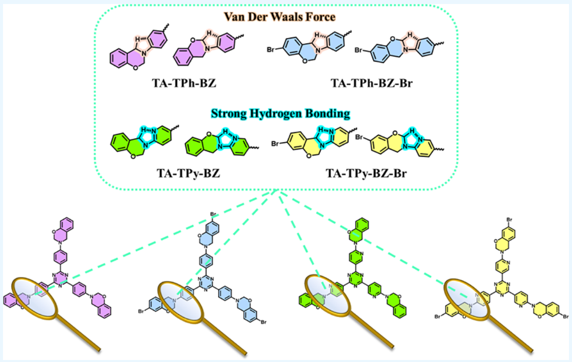

**KEYWORDS:** *triazine, benzoxazine, hydrogen bonding, thermal stability, activation energy, thermal ring-opening polymerization, density functional theory*

## ■ INTRODUCTION

In recent research, benzoxazine resins (BZ) have emerged as highly promising thermosetting resins because of their outstanding properties, including dimensional stability, excellent thermal stability,[1−3] extraordinary electrical resistance,[4] low surface-free energy,[5−7] superior flame retardancy,[8] and resilient molecular design.[9,10] These materials, which feature six-membered heterocyclic rings, are generally synthesized via the Mannich condensation reaction involving an aldehyde derivative, a primary aromatic or aliphatic amine, and a phenolic derivative.[11−17] Moreover, the physical and chemical properties of polybenzoxazines (PBZs) can be precisely tuned by incorporating various functional groups, for instance, allyl, alkynyl, bromophenyl, hydroxyl, nitrile, furan, phenyl, or fluorescent moieties, or by introducing strong hydrogen bonding segments into the benzoxazine monomers.[18−28] As a consequence, the upcoming generation of outstanding-durability polymers, identified as polybenzoxazines (PBZs), combines ease of synthesis with a range of unique properties that make them ideal for advanced applications such as aerospace technologies, battery electrodes, carbon dioxide adsorption, coatings, and electronic components.[29−37]

In seeking new routes to enhance PBZ performance, triazine (TA) is a six-membered aromatic heterocyclic compound containing nitrogen and ranks among the oldest known organic molecules; some derivatives have been known for over a century.[38−40] Initially introduced as sym-TAs, they have now commonly emerged simply as TAs. The molecular structure of TA features a slightly distorted hexagonal ring, as the C−N−C bond angles are commonly a bit less than 120°, a trait shared by many heterocyclic systems.[41−43] Importantly, substituents have little effect on its bond lengths and ring angles. Compared to the other six-membered heteroaromatic rings with nitrogen,

**Received:** June 4, 2025
**Revised:** July 15, 2025
**Accepted:** July 16, 2025
**Published:** July 23, 2025

https://doi.org/10.1021/acsapm.5c02017

Scheme 1. Synthesis of (d) TA-TPh-BZ and (h) TA-TPh-BZ-Br Monomers from 4-Aminobenzonitrile, (a) TA-TPh-3NH$_2$, (b) TA-TPh-SF, and (c) TA-TPh-HBA; (f) TA-TPh-SF-Br, and (g) TA-TPh-HBA-Br; Analogous Pyridine Series: Synthesis of (e) TA-TPy-BZ and (i) TA-TPy-BZ-Br Monomers from 6-Aminonicotinonitrile, (a) TA-TPy-3NH$_2$, (b) TA-TPy-SF, and (c) TA-TPy-HBA; (f) TA-TPy-SF-Br, and (g) TA-TPy-HBA-Br

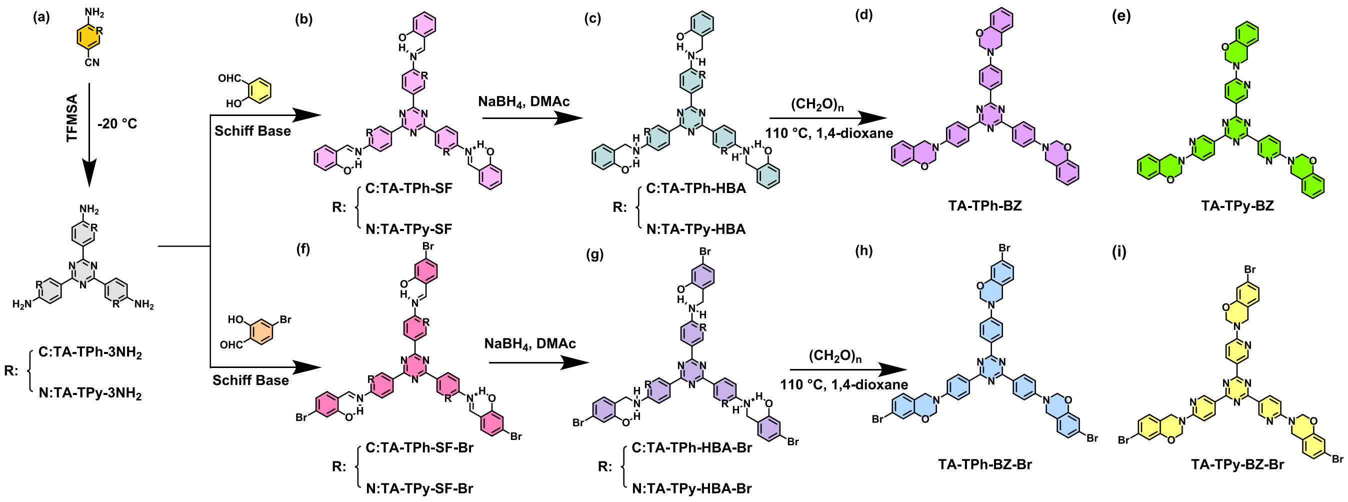

TA is notably $\pi$ electron-deficient, which makes it more susceptible to nucleophilic attack.[44−47] These electronic characteristics render TA a key moiety in both chemical synthesis and optical applications.[48,49] For instance, TA derivatives have been successfully employed as efficient electron transport materials in organic electronics due to their strong electron affinity, excellent optoelectronic properties, and robust thermal stability.[50,51] Moreover, the inherent $C_3$ symmetry of TA allows for the construction of diverse star-shaped molecules, porous materials, and molecular cages, making it highly valuable in chemistry.[51,52] By embedding TA units within BZ monomers, we seek to merge the outstanding thermal and mechanical stability of PBZs with the electronic and structural advantages of triazine cores. This hybrid approach promises materials that not only withstand extreme conditions but also offer tunable electronic and morphological features. Despite these potential benefits, triazinebenzoxazine hybrids remain largely unexplored. In this work, we therefore report the first systematic synthesis and characterization of high-purity, trifunctional triazine-based benzoxazine monomers, and we investigate how their triazine content and, subsequently, additional pyridine or bromine substituents modulate polymerization kinetics, thermal behavior, and chain-packing organization.

Pyridine compounds are characterized by a six-membered heterocyclic ring consisting of five carbon atoms and one nitrogen atom. Due to these unique characteristics, pyridine serves as a crucial building block in the synthesis of various organic compounds, including pharmaceuticals,[53] and agrochemicals.[54] Additionally, pyridine derivatives, which contain diverse substituents at different positions on the ring, exhibit varying reactivity based on the nature and location of these substituents. This structural versatility makes pyridine and its derivatives indispensable in numerous chemical processes, underscoring their significance in synthetic chemistry. Despite the broad utility of pyridine in organic synthesis, research on benzoxazines featuring pyridine functional groups within the main chain and hyperbranched remains limited. Most existing synthetic approaches involve modifications at the para position using amino (−NH$_2$) functional groups to obtain benzoxazines.[55−57] Expanding the scope of pyridine-functionalized benzoxazines could offer new avenues for tailoring material properties and enhancing performance in advanced applications. Incorporating pyridine moieties into benzoxazine structures offers several key benefits. Pyridine-containing polybenzoxazines exhibit higher thermal degradation temperatures, making them ideal for high-temperature use.[57−59] Their rigid aromatic−heterocyclic framework increases cross-link density, enhancing mechanical strength and stiffness. The polarity of pyridine rings improves adhesion to polar substrates and compatibility in composites. Additionally, the pyridine nitrogen provides coordination sites for metal ions, enabling the creation of functional hybrid materials with adjustable properties. To our knowledge, this study is the first to synthesize high-purity triazine-based benzoxazine monomers and provide a comprehensive analysis of their polymerization kinetics. Additionally, we elucidate the role of noncovalent interactions involving pyridine moieties and bromine substitution, contributing to a deeper understanding of their impact on the polymerization process.

In this study, we report the first high-purity syntheses of two trifunctional triazine-based benzoxazine monomer series, TA-TPh-3NH$_2$ and TA-TPy-3NH$_2$, via TFMSA-mediated cyclotrimerization of 4-aminobenzonitrile and 6-aminonicotinonitrile, respectively. For the aniline-derived TA-TPh-3NH$_2$, a straightforward one-pot sequence of Schiff base formation (to TA-TPh-SF and TA-TPh-SF-Br), hydride reduction (to TA-TPh-HBA and TA-TPh-HBA-Br), and Mannich condensation (to TA-TPh-BZ and TA-TPh-BZ-Br) delivered all six target derivatives under standard laboratory conditions. By contrast, the lower nucleophilicity and basicity of the pyridine amine in TA-TPy-3NH$_2$ necessitated a Dean−Starkassisted condensation to generate the corresponding Schiff base intermediates (TA-TPy-SF and TA-TPy-SF-Br) before applying identical reduction and Mannich cyclization steps to obtain TA-TPy-HBA, TA-TPy-HBA-Br, TA-TPy-BZ, and TA-TPy-BZ-Br.[60] Comprehensive characterization, which encompassed FTIR, NMR, DSC, TGA, XRD, ESIMS, and computational DFT/RDG/MESP analyses, then elucidated how intramolecular hydrogen bonding in the pyridine series and bromine substitution modulate ring opening polymerization, thermal behavior, electronic structure, and local chain packing, thereby establishing new design principles for advanced benzoxazine materials.

## EXPERIMENTAL SECTION

**Materials.** Salicylaldehyde (99%), paraformaldehyde [$(CH_2O)_n$, 98%], 1,4-dioxane (DO, 98%), ethyl acetate (EA, 99%), ethanol (99.5%), and toluene were purchased from Alfa Aesar. Dimethylformamide (DMF) and dimethylacetamide (DMAc) were procured from DUKSAN. Fisher Chemical was the merchant for chloroform (99.8%). Matrix Scientific was the supplier for 4-aminobenzonitrile (98%). trifluoromethanesulfonic acid [TFMSA, (99%)], 6-aminonicotinonitrile (97%), and 4-bromo-2-hydroxybenzaldehyde (97%) were purchased from Sigma-Aldrich. Sodium hydroxide (NaOH, 97%) and magnesium sulfate anhydrous ($MgSO_4$, 99%) were acquired from SHOWA. Sodium borohydride ($NaBH_4$, 98%) was procured from Thermo Scientific.

*Synthesis of 4,4″,4‴-(1,3,5-Triazine-2,4,6-triyl)trianiline (TA-TPh-3NH$_2$).* 4-Aminobenzonitrile (2 g, 16.92 mmol) was combined with TFMSA (5.23 mL, 59.24 mmol) in 50 mL of chloroform under a nitrogen atmosphere. The reaction mixture was carried out at −20 °C for 24 h in a Dewar flask containing a methanol/liquid nitrogen cooling system. Upon completion, the resulting yellow oil layer was discrete and diluted with 100 mL of cold water. The pH of the mixture was adjusted to 8−12 using a 0.2 M $NaOH_{(aq)}$, which precipitated a yellow solid. The solid was filtered and washed with ethanol three times, yielding 1.66 g (4.68 mmol) of a cream-yellow solid [Yield = 83%, Scheme 1a].

**Synthesis of TA-TPh-SF and TA-TPh-SF-Br.** TA-TPh-3NH$_2$ (1 g, 2.82 mmol) was combined with salicylaldehyde (0.88 mL, 8.47 mmol) or 4-bromo-2-hydroxybenzaldehyde (1.76 g, 8.75 mmol) in 50 mL of ethanol under a nitrogen atmosphere. The mixture was reacted at 80 °C for 24 h. The resulting mixture was then filtered and washed with water and ethanol. Amber-colored solids dried in the vacuum oven and yielded 1.73 g (2.59 mmol) [Yield = 92%, Scheme 1b] or 2.29 g (2.53 mmol) [Yield = 90%, Scheme 1f].

**Synthesis of TA-TPh-HBA and TA-TPh-HBA-Br.** TA-TPh-SF (1 g, 1.49 mmol) or TA-TPh-SF-Br (1 g, 1.10 mmol) was reacted with $NaBH_4$ (0.62 g, 16.50 mmol; 0.41 g, 11.06 mmol) in 5 mL of DMAc under a nitrogen atmosphere. After the reaction, the mixture was poured into 500 mL of water and filtered. The resulting residues were dried in a vacuum oven, yielding 0.97 g (1.44 mmol) of a butter-colored solid. [TA-TPh-HBA, yield = 96%, Scheme 1c] and yielding 0.90 g (0.99 mmol) of an orange solid [TA-TPh-HBA-Br, yield = 90%, Scheme 1g].

**Synthesis of TA-TPh-BZ and TA-TPh-BZ-Br.** TA-TPh-HBA (0.5 g, 0.74 mmol) or TA-TPh-HBA-Br (0.5 g, 0.55 mmol) was reacted with $(CH_2O)_n$ (0.08 g, 2.60 mmol; 0.05 g, 1.76 mmol) in 50 mL of DO under a nitrogen atmosphere. The mixture was reacted at 110 °C for a full day. Afterward, the solvent was removed using a rotary evaporator, and the remaining residues were dried in a vacuum oven, which yielded 0.47 g (0.66 mmol) of light yellowish-colored solids [TA-TPh-BZ, yield = 90%, Scheme 1d] or yielded 0.45 g (0.48 mmol) of butter-colored solids [TA-TPh-BZ-Br, yield = 88%, Scheme 1h].

**Synthesis of 5,5″,5′″-(1,3,5-Triazine-2,4,6-triyl)tris(pyridin-2-amine) (TA-TPy-3NH$_2$).** 6-Aminonicotinonitrile (2 g, 16.78 mmol) was reacted with TFMSA (5.18 mL, 58.76 mmol) in 50 mL of chloroform under a nitrogen atmosphere. The reaction was conducted at −20 °C for 24 h in a Dewar flask cooled with a methanol/liquid nitrogen system. Afterward, the mixture was separated and diluted with 100 mL of cold water. The pH was adjusted to a range of 8−12 with a 0.2 M $NaOH_{(aq)}$, bringing about the precipitation of a dark gray solid. The gray precipitates were collected by filtration and washed with ethanol. The crude product was recrystallized by THF and dried to obtain 1.56 g (4.37 mmol) of a pale pink solid [Yield = 78%, Scheme 1(a)].

**Synthesis of TA-TPy-SF and TA-TPy-SF-Br.** TA-TPy-3NH$_2$ (1 g, 2.79 mmol) was reacted with either salicylaldehyde (0.88 mL, 8.39 mmol) or 4-bromo-2-hydroxybenzaldehyde (1.76 g, 8.75 mmol) in 50 mL of DMF and toluene under a nitrogen atmosphere in the Dean−Stark procedure. The reaction mixture was heated at 100 °C for 24 h. After completion, the solvent was removed using a rotary evaporator, and the residues were washed with water and ethanol. The resulting solids were dried in a vacuum oven. When salicylaldehyde was used, the reaction yielded 1.67 g (2.49 mmol) of a tangerine yellow solid [TA-TPy-SF, yield = 89%, Scheme 1b]. In contrast, using 4-bromo-2-hydroxybenzaldehyde produced 2.27 g (2.50 mmol) of an orange solid [TA-TPy-SF-Br, yield = 90%, Scheme 1f].

**Synthesis of TA-TPy-HBA and TA-TPy-HBA-Br.** TA-TPy-SF (1 g, 1.49 mmol) or TA-TPy-SF-Br (1 g, 1.10 mmol) was reacted with $NaBH_4$ (0.62 g, 16.42 mmol; 0.46 g, 12.13 mmol) in 5 mL of DMAc under a nitrogen atmosphere. Afterward, the mixture was poured into 500 mL of water and filtered. The resulting solid was dried in a vacuum oven, yielding 0.77 g (1.13 mmol) of a pale-yellow solid [TA-TPy-HBA, yield = 76%, Scheme 1c] or 0.56 g (0.62 mmol) of cornsilk-colored solid [TA-TPy-HBA-Br, yield = 56%, Scheme 1g].

**Synthesis of TA-TPy-BZ and TA-TPy-BZ-Br.** TA-TPy-HBA (0.5 g, 0.74 mmol) or TA-TPy-HBA-Br (0.5 g, 0.54 mmol) was reacted with $(CH_2O)_n$ (0.07 g, 2.59 mmol; 0.06 g, 1.91 mmol) in 50 mL of DO under a nitrogen atmosphere. The reaction was reacted at 110 °C for 24 h. Upon completion, the solvent was removed by a rotary evaporator, and the remaining residue was dried in a vacuum oven, which yielded 0.42 g (0.59 mmol) of a cornsilk-colored solid [TA-TPy-BZ, yield = 81%, Scheme 1e or 0.38 g (0.40 mmol) of light vermilion solid. [TA-TPy-BZ-Br, yield = 74%, Scheme 1i].

## RESULTS AND DISCUSSION

**Synthesis and Characterization of Triazine-Based Benzoxazines.** Scheme 1 outlines the divergent synthetic strategies used to access two series of triazine-based benzoxazine monomers. In the TPh series, TA-TPh-3NH$_2$ was prepared by cyclotrimerization of 4aminobenzonitrile and subsequently converted to TA-TPh-BZ and its brominated analogue (TA-TPh-BZ-Br) through a three-step sequence comprising Schiff base formation, reduction, and Mannich condensation. By contrast, the inherently lower nucleophilicity of the pyridine-derived amino group in TA-TPy-3NH$_2$ rendered a direct, one-step benzoxazine synthesis impractical. Consequently, TA-TPy-BZ and TA-TPy-BZ-Br were instead obtained through an analogous three-step protocol, Schiff base condensation, hydride reduction, and Mannich cyclization, starting from 6aminonicotinonitrile and as similarly depicted in Scheme 1a-i. The molecular structures of TA-TPh-3NH$_2$, TA-

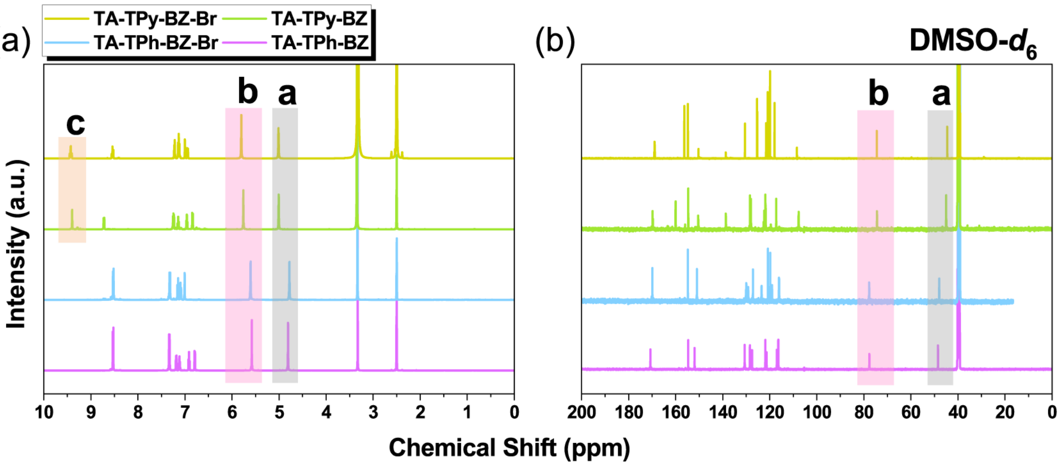

**Figure 1.** (a) $^1$H NMR and (b) $^{13}$C NMR of TA-TPh-BZ, TA-TPh-BZ-Br, TA-TPy-BZ, and TA-TPy-BZ-Br.

TPh-SF, TA-TPh-HBA, TA-TPh-BZ, TA-TPh-SF-Br, TA-TPh-HBA-Br and TA-TPh-BZ-Br, as presented in Figures S1a-d and S2a-d. Figures S3a-d and S4a-d present the chemical structures of TA-TPy-3NH$_2$, TA-TPy-SF-Br, TA-TPy-HBA-Br, TA-TPy-BZ-Br, TA-TPy-SF-Br, TA-TPy-HBA-Br and TA-TPy-BZ-Br. Figures S1e, S2e, S3e, and S4e illustrate FTIR analysis of the starting materials, revealing that the TA-TPh-3NH$_2$ monomer manifests characteristic peaks for primary amine groups and sp$^2$ C−H bonds. Specifically, symmetric and asymmetric N−H stretching vibrations emerge at 3324 cm$^{-1}$ and 3462 cm$^{-1}$, respectively, while the sp$^2$ C−H stretching vibration is observed at 3030 cm$^{-1}$. In contrast, the TA-TPy-3NH$_2$ monomer manifests symmetric and asymmetric N−H stretches at 3342 cm$^{-1}$ and 3441 cm$^{-1}$, respectively, with the sp$^2$ C−H stretches at 3051 cm$^{-1}$ and the pyridine C═N stretches at 1571 cm$^{-1}$. Post the Schiff base reaction, the FTIR spectra of the TA-TPh-SF, TA-TPh-SF-Br, TA-TPy-SF, and TA-TPy-SF-Br intermediates unveil broad absorption bands for the hydroxyl moiety between 3050 and 3750 cm$^{-1}$, along with a sharp imine absorption band in the range of 1570 to 1595 cm$^{-1}$. Subsequent reduction to yield the hydroxybenzylamine derivatives (TA-TPh-HBA, TA-TPh-HBA-Br, TA-TPy-HBA, and TA-TPy-HBA-Br) is validated by the evanescence of the imine peaks and the emergence of new N−H absorption bands between 3405 and 3420 cm$^{-1}$. Finally, the formation of the oxazine ring through Mannich condensation is validated by distinct FTIR signals. For TA-TPh-BZ, the characteristic peaks at 949 cm$^{-1}$ and 1255 cm$^{-1}$ confirmed the oxazine ring structure, while TA-TPh-BZ-Br shows the peaks at 953 cm$^{-1}$ and 1269 cm$^{-1}$. Similarly, TA-TPy-BZ was confirmed by absorption peaks at 968 cm$^{-1}$ and 1258 cm$^{-1}$, and TA-TPy-BZ-Br displayed peaks at 966 cm$^{-1}$ and 1250 cm$^{-1}$. Additionally, the characteristic triazine signals are observed at ca. 1605 cm$^{-1}$ and 1375 cm$^{-1}$ in all benzoxazine monomers. The $^1$H NMR spectra of the starting monomers are presented in Figures S1f, S2f, S3f, and S4f. For TA-TPh-3NH$_2$, characteristic signals corresponding to aromatic C−**H** and amino protons are observed at 8.34 ppm, 6.68 ppm, and 5.90 ppm. In contrast, TA-TPy-3NH$_2$ exhibits distinct aromatic C−**H** and amino proton signals at 9.19 ppm, 8.49−8.50 ppm, 6.56−6.58 ppm, and 6.79 ppm. Following the Schiff base reaction with either salicylaldehyde or 4-bromo-2-hydroxybenzaldehyde, the amino proton signals disappear, and new signals for the hydroxyl (O−**H**) and imine (N═C—**H**) protons emerge. Specifically, in TA-TPh-SF, these appear at 12.86 ppm and 9.05 ppm, distinctively; in TA-TPh-SF-Br at 13.16 ppm and 9.08 ppm; in TA-TPy-SF at 10.70 ppm and 7.64 ppm; and in TA-TPy-SF-Br at 11.1 ppm and 7.57 ppm. In addition, the aromatic C−**H** signals are observed over a broad range from 6.50 to 9.20 ppm. Notably, the imine proton in TPy derivatives is more shielded than those in the TPh derivatives. This is likely attributed to the formation of N═C−H···N hydrogen bonds between the imine and pyridine groups, resulting in an imidazole-like structure. Further details of this interaction are discussed in the Density Functional Theory (DFT) section. After the reduction reaction to produce hydroxybenzylamine (HBA) derivatives (TA-TPh-HBA, TA-TPh-HBA-Br, TA-TPy-HBA, and TA-TPy-HBA-Br), the signals for imine protons vanished, while new signals for amino and N−C−**H** protons appeared in the ranges of 5.89−7.83 ppm and 4.25−4.51 ppm, distinctively. The aromatic C−**H** signals in these derivatives are observed between 6.67 and 9.26 ppm and are more shielded compared to the imine signals, owing to the electron-donating effect of the NH moieties. Finally, after the Mannich condensation reaction, the formation of the benzoxazine structure is confirmed by the appearance of characteristic signals. In TA-TPh-BZ, Figures 1a and S5 reveal a singlet at 4.80 ppm corresponding to the Ar−C**H$_2$**−N moiety and a singlet at 5.58 ppm corresponding to the O−C**H$_2$**−N moiety, while TA-TPh-BZ-Br manifests signals at 4.78 ppm and 5.60 ppm [Figure S6], respectively. For the pyridine-based monomers, TA-TPy-BZ shows signals at 5.00 ppm for the Ar−C**H$_2$**−N moiety and 5.75 ppm for the O−C**H$_2$**−N moiety [Figure S7], while TA-TPy-BZ-Br discloses signals at 5.01 ppm and 5.80 ppm [Figure S8], distinctively. Moreover, in the TPh series, aromatic C−**H** signals appear in the range of 6.80 to 8.53 ppm, whereas in the TPy series, they are observed between 6.85 and 9.42 ppm. Figures S1g, S2g, S3g, and S4g present the $^{13}$C NMR spectra for the starting monomers and their derivatives. For the TA-TPh-3NH$_2$ compound, the characteristic signals corresponding to the phenyl carbons appear between 113 and 153 ppm, along with a signal at 170 ppm attributed to the triazine groups. Similarly, the TA-TPy-3NH$_2$ monomer exhibits the signals of aromatic carbons ranging from 108 to 163 ppm and a triazine signal at 170 ppm. After the Schiff base reaction, the SF derivatives manifest signals spanning 105−170 ppm, which can be assigned to the aromatic carbons, N═**C** bonds, and triazine groups. However, no signals were observed for TA-TPh-SF-Br, likely on account of its poor solubility. The HBA derivatives unveil signals for the aromatic carbons and triazine groups in the range of 110−170 ppm, along with a distinct signal at 41−42 ppm corresponding to the NH−$\underline{\text{C}}$H moieties. Notably, the signals associated with the N═$\underline{\text{C}}$ groups vanish. Finally, after the Mannich condensation reaction, the formation of the oxazine ring is confirmed by distinctive signals. In TA-TPh-BZ and TA-TPh-BZ-Br, the oxazine ring signals are observed at 77 ppm and 48 ppm, respectively; in TA-TPy-BZ, they emerge at 74 ppm and 45 ppm; and in TA-TPy-BZ-Br, at 75 ppm and 45 ppm. Additionally, the aromatic carbons and triazine groups continue to be observed between 107 and 170 ppm, as shown in Figure 1b.

Moreover, elemental analysis and electrospray ionization mass spectrometry (ESI-MS) were employed to verify the molecular structures and purity of the synthesized benzoxazine monomers. As summarized in Table S1, the elemental compositions of the monomers showed excellent agreement with their theoretical values, confirming the successful incorporation of the desired functional groups. Elemental analysis of TA-TPh-BZ revealed carbon, nitrogen, and hydrogen contents of 75.17 wt %, 10.35 wt %, and 5.05 wt %, respectively. For TA-TPh-BZ-Br, the carbon and hydrogen contents decreased to 59.98 wt % and 3.21 wt %, respectively, while the nitrogen content remained relatively stable at 9.81 wt %. These changes are consistent with substituting a hydrogen atom with a bromine atom. For the pyridine-containing analogues, TA-TPy-BZ exhibited 70.82 wt % carbon, 17.73 wt % nitrogen, and 4.61 wt % hydrogen. In contrast, its brominated derivative, TA-TPy-BZ-Br, showed reduced values of 53.71 wt % carbon, 14.12 wt % nitrogen, and 3.08 wt % hydrogen. These findings were further supported by ESI-MS analyses, as shown in Figures S9−S12. TA-TPh-BZ presented two prominent peaks at $m/z$ 697 and 709, corresponding to $[\text{TA-TPh-BZ} - \text{CH}_2 + 3\text{H}]^+$ and $[\text{TA-TPh-BZ} + \text{H}]^+$ [Scheme S2 and Figure S9], while TA-TPh-BZ-Br displayed peaks at $m/z$ 909 and 944, attributed to $[\text{TA-TPh-BZ-Br} - \text{Br} - 3\text{H} + 2\text{Na}]^{2-}$ and $[\text{TA-TPh-BZ-Br}-\text{H}]^-$ [Figure S10]. For the TPy series, TA-TPy-BZ showed a peak at $m/z$ 712, corresponding to $[\text{TA-TPy-BZ} + \text{H}]^+$ [Figure S11], and TA-TPy-BZ-Br exhibited a peak at $m/z$ 965, consistent with $[\text{TA-TPy-BZ-Br} - 6\text{H} + \text{Na}]^{5-}$ [Figure S12]. Together, the elemental and spectrometric data confirm the accurate synthesis and structural integrity of the targeted triazine-based benzoxazine monomers. Furthermore, DSC analysis further supports successful synthesis. The uncuring TA-TPh-BZ monomer exhibits a melting point ($T_m$) at 229 °C and undergoes a ring-opening polymerization (ROP) reaction at 275 °C, while TA-TPh-BZ-Br shows the ROP reaction at 260 °C. In the TPy series, the TA-TPy-BZ monomer displays a $T_m$ of 155 °C with the ROP event at 283 °C, and TA-TPy-BZ-Br evidence a $T_m$ at 206 °C and the ROP reaction at 288 °C as displayed in Figure 2.

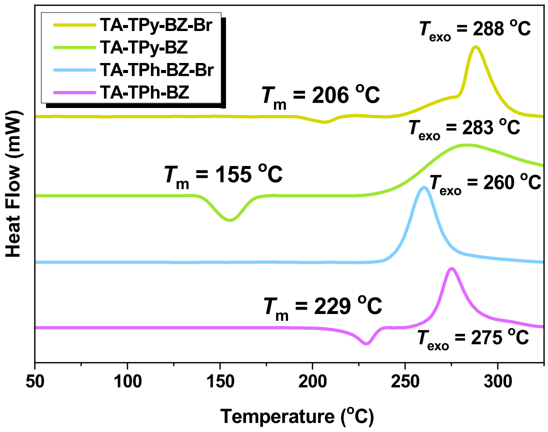

**Figure 2.** DSC exothermic curves of the triazine-based benzoxazines.

**Thermal Ring-Opening Polymerization of Triazine-Based Benzoxazines.** Figures S13a-d and 3 illustrate the FTIR spectra and DSC profiles, respectively, of TA-TPh-BZ, TA-TPh-BZ-Br, TA-TPy-BZ, and TA-TPy-BZ-Br under various thermal treatment conditions. For the TPh series, the thermal curing of TA-TPh-BZ leads to pronounced changes in its FTIR and DSC profiles, confirming efficient ring-opening polymerization and network formation. In the FTIR spectra [Figure S13a], the characteristic oxazine-ring absorption at 949 cm$^{-1}$ gradually diminishes as the curing temperature rises from 25 to 250 °C, disappearing completely by 280 °C. At the same time, a broad phenolic O−H stretching band emerges and intensifies, directly evidencing conversion of oxazine moieties into phenolic networks. These spectral observations align closely with the DSC data [Figure 3a and Table S2], where the $T_m$ and ROP exotherm both shift to lower temperatures at 220 °C, only for the melting endotherm to vanish and the exotherm to shift to higher temperatures upon further heating to 250 °C. Above 280 °C, the disappearance of the ROP peak indicates the completion of network formation, yielding a highly cross-linked poly(TA-TPh-BZ) as depicted in Figure S14a. The detailed mechanism by which the triazine-benzoxazine undergoes thermal polymerization is illustrated in Scheme S1.[61,62] Similarly, the FTIR spectrum of TA-TPh-BZ-Br in Figure S13b reveals that the oxazine ring absorption band at 953 cm$^{-1}$ decreases as the curing temperature increases from 25 °C to 250 °C, disappearing entirely at 280 °C. Concurrently, a broad phenolic O−H stretching band appears and grows in intensity, providing clear evidence that the oxazine rings undergo ROP reaction to yield a phenolic network. This trend is corroborated by the DSC results in Figure 3b and Table S3. As the temperature reaches 220 °C, the ROP peaks shift to lower temperatures; however, when further increased to 280 °C, the ROP peaks shift to higher temperatures, and ultimately, beyond 280 °C, the disappearance of the ROP peaks corroborates the formation of a highly cross-linked poly(TA-TPh-BZ-Br) network, as depicted in Figure S14b. In the TPy series, the FTIR spectrum of TA-TPy-BZ [Figure S13c] demonstrates that the oxazine ring absorption band at 968 cm$^{-1}$ gradually decreases as the curing temperature rises from 25 °C to 250 °C, disappearing entirely at 280 °C, which agrees with the DSC results illustrated in Figure 3c and Table S4. A broad phenolic O−H stretching band appears and grows in intensity, providing unequivocal evidence that the oxazine rings undergo ROP to form a cross-linked phenolic network. Strikingly, at 220 °C, the melting point is no longer detectable, and the ROP peaks shift to lower temperatures; however, as the temperature increases further from 220 °C to 250 °C, the ROP peaks shift to higher temperatures. Beyond 280 °C, the absence of the ROP peaks indicates the formation of a highly cross-linked poly(TA-TPy-BZ) network, as depicted in Figure S14c. For TA-TPy-BZ-Br, the FTIR data in Figure S13d exhibit that the absorption band of the oxazine ring at 966 cm$^{-1}$ gradually diminishes with escalating temperature from 25 °C to 250 °C, vanishing

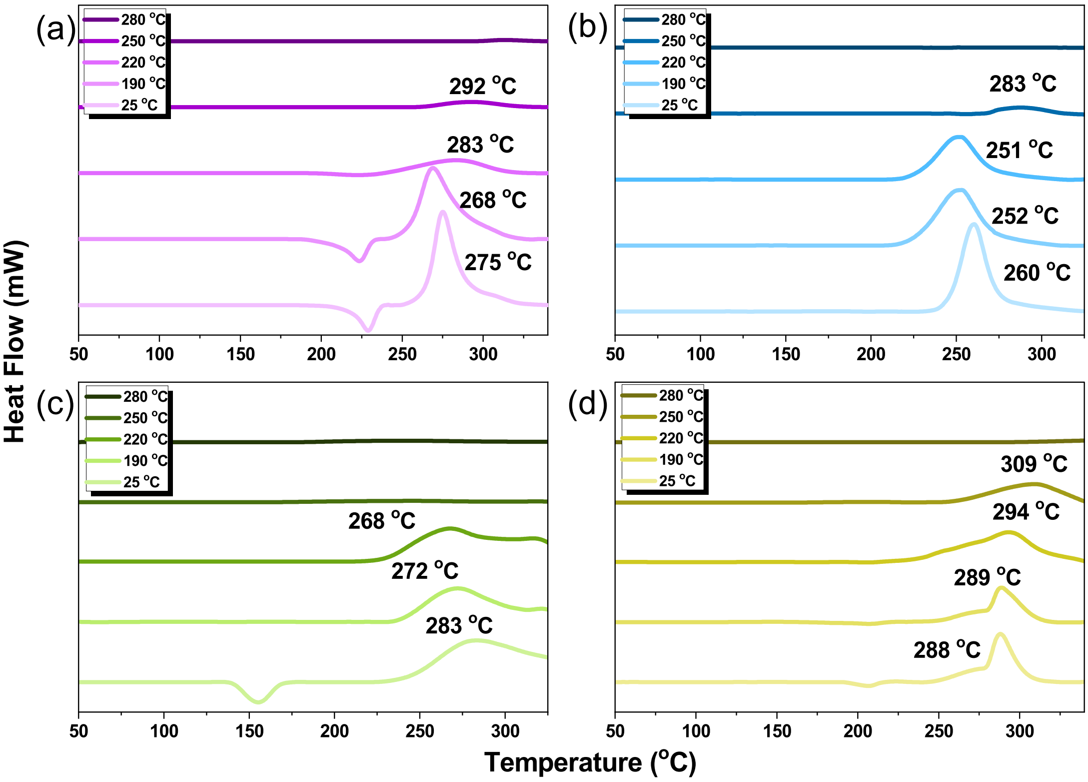

**Figure 3.** Dynamic DSC profiles of (a) TA-TPh-BZ, (b) TA-TPh-BZ-Br, (c) TA-TPy-BZ, and (d) TA-TPy-BZ-Br.

completely at 280 °C. Simultaneously, the development and increasing intensity of the broad O−H stretching band provide definitive proof of oxazine ring-opening polymerization leading to a cross-linked phenolic structure. This trend is consistent with the DSC results presented in Figure 3d and Table S5. Notably, as the temperature reaches 280 °C, the ROP peaks shift to higher temperatures and eventually vanish, verifying the formation of a highly cross-linked poly(TA-TPy-BZ-Br) network, as illustrated in Figure S14d.

Figure S15 reveals that the unprocessed TA-TPh-BZ monomer exhibits a temperature at 10% weight loss ($T_{d10}$) of 451 °C and a char yield of 57 wt %. After thermal treatment, its $T_{d10}$ values increase moderately to 475, 479, 480, and 514 °C, with corresponding char yields of 60, 63, 65, and 67 wt % [Figure S16 and Table S2]. Similarly, Figure S17 indicates that the unprocessed TA-TPh-BZ-Br monomer has a $T_{d10}$ of 407 °C and a char yield of 52 wt %, which rose to 412, 418, 421, and 428 °C with char yields of 54, 55, 56, and 57 wt % after thermal treatment [Figure S18 and Table S3]. In the TPy series, Figure S19 exhibits that the unprocessed TA-TPy-BZ monomer shows a $T_{d10}$ of 441 °C and a char yield of 53 wt %; after thermal treatment, the $T_{d10}$ values increase to 443, 452, 462, and 497 °C, with char yields of 56, 57, 58, and 60 wt % [Figure S20 and Table S4]. Furthermore, Figure S21 reveals that the unprocessed TA-TPy-BZ-Br monomer has a $T_{d10}$ of 354 °C and a char yield of 49 wt %, which increases to 401, 422, 434, and 442 °C with char yields of 50, 52, 55, and 57 wt % after treatment [Figure S22 and Table S5]. Integrating these data into Figure S14e,f reveals that, following 280 °C heat treatment, TA-TPh-BZ displays the highest $T_{d10}$ and char yield. In contrast, the incorporation of a bromine atom significantly decreases both the $T_{d10}$ and the char yield, while the introduction of a pyridine functional group results in a slight change in these thermal parameters.

**Density Functional Theory (DFT) and Hydrogen Bonding Influence of Triazine-Based Monomers.** Table S6 indicates that the $^1$H NMR spectra for both the TPh and TPy Schiff base series suggest a weak interaction involving the imine group. Notably, the pyridine group, which owes to its nitrogen atom, forms a weak hydrogen bond, while the benzene group engages primarily in Van Der Waals interactions. This difference in interaction alters the configuration between the pyridine and imine groups, resulting in an imidazole-like arrangement. Interestingly, although intramolecular hydrogen bonding typically causes proton deshielding, evidenced by the hydroxyl groups in both series appearing at chemical shifts >10.5 ppm, the formation of an imidazole-like structure induces an aromatic ring current effect that increases proton shielding. Consequently, the signals of imine and phenolic protons in the TPy series appear at lower chemical shifts compared to those in the TPh series. In contrast, the incorporation of a bromine atom leads to slight deshielding of the phenolic proton. Moreover, the energy of the hydrogen bonds ($E_{HB}$) for the monomers was calculated using Multiwfn software on geometries optimized at the B3LYP-D3(BJ)/6−31+G(d,p) level, further corroborating these subtle electronic effects.[63] Both experimental and computational results confirm that the hydroxyl group forms a stable intramolecular hydrogen bond with the nitrogen atom (O−H···N) in TA-TPh-SF, TA-TPh-SF-Br, TA-TPy-SF, and TA-TPy-SF-Br, with $E_{HB}$ values of 10.49, 10.84, 10.67, and 10.92 kcal/mol, respectively [Table S7]. This finding recommends that the incorporation of a bromine atom and the presence of pyridine moieties slightly affect hydrogen bond interactions.

Post the reduction and Mannich condensation reactions, the imidazole-like structure is disrupted, and the aromatic ring current effect disappears. In the hydroxybenzylamine series, the TPy derivative exhibits a chemical shift that is 0.21 ppm higher

Table 1. Proton Record, $E_a$, and $E_{HB}$ between the Oxazine Ring in Triazine-Based Benzoxazine

| | Protons of oxazine ring (ppm) | | $E_a$ (kJ/mol) | | $E_{HB}$ (kcal/mol) | |
|---|---|---|---|---|---|---|
| | Ar-$\mathbf{CH_2}$-N | O-$\mathbf{CH_2}$-N | Kissinger | Ozawa | | |
| TA-TPh-BZ | 4.80 | 5.58 | 104.14 | 113.00 | | |
| TA-TPh-BZ-Br | 4.78 | 5.60 | 123.19 | 131.87 | | |
| TA-TPy-BZ | 5.00 | 5.75 | 110.35 | 119.36 | 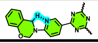<br>3.52 | 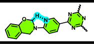<br>3.49 |
| TA-TPy-BZ-Br | 5.01 | 5.80 | 128.27 | 137.38 | 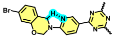<br>3.56 | 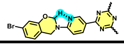<br>3.50 |

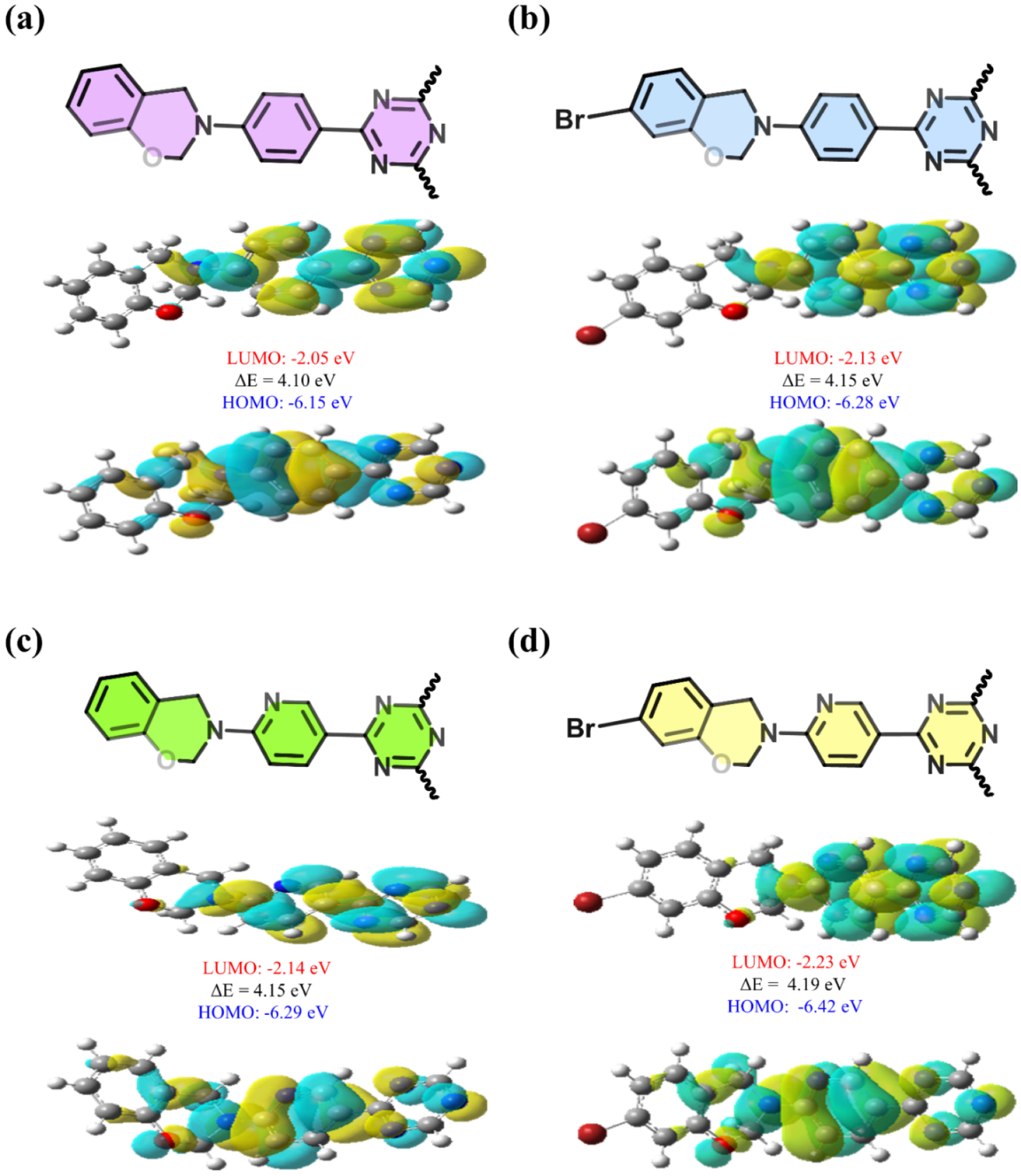

**Figure 4.** HOMO and LUMO isosurface maps of (a) TA-TPh-BZ, (b) TA-TPh-BZ-Br, (c) TA-TPy-BZ, and (d) TA-TPy-BZ-Br along with their energies calculated at the B3LYP-D3(BJ)/6−31+G(d,p) level.

than that of the TPh derivative [Table S8]. Similarly, in the benzoxazine series, the TPy derivative shows a chemical shift approximately 0.2 ppm higher than its TPh counterpart. These deshielding differences are attributed to intramolecular hydrogen bonding between the hydroxybenzylamine unit or oxazine ring and the pyridine moiety. Furthermore, both experimental and computational results demonstrate that the oxazine ring forms weak intramolecular hydrogen bonds with the pyridine moieties in TA-TPy-BZ. Specifically, the $E_{HB}$ values for the interactions between the Ar−$\mathbf{CH_2}$−N group and the pyridine and between the O−$\mathbf{CH_2}$−N group and the pyridine are 3.52 and 3.49 kcal/mol, respectively. In TA-TPy-BZ-Br, these values are 3.56 and 3.50 kcal/mol, respectively [Table 1]. These findings suggest that bromine incorporation slightly

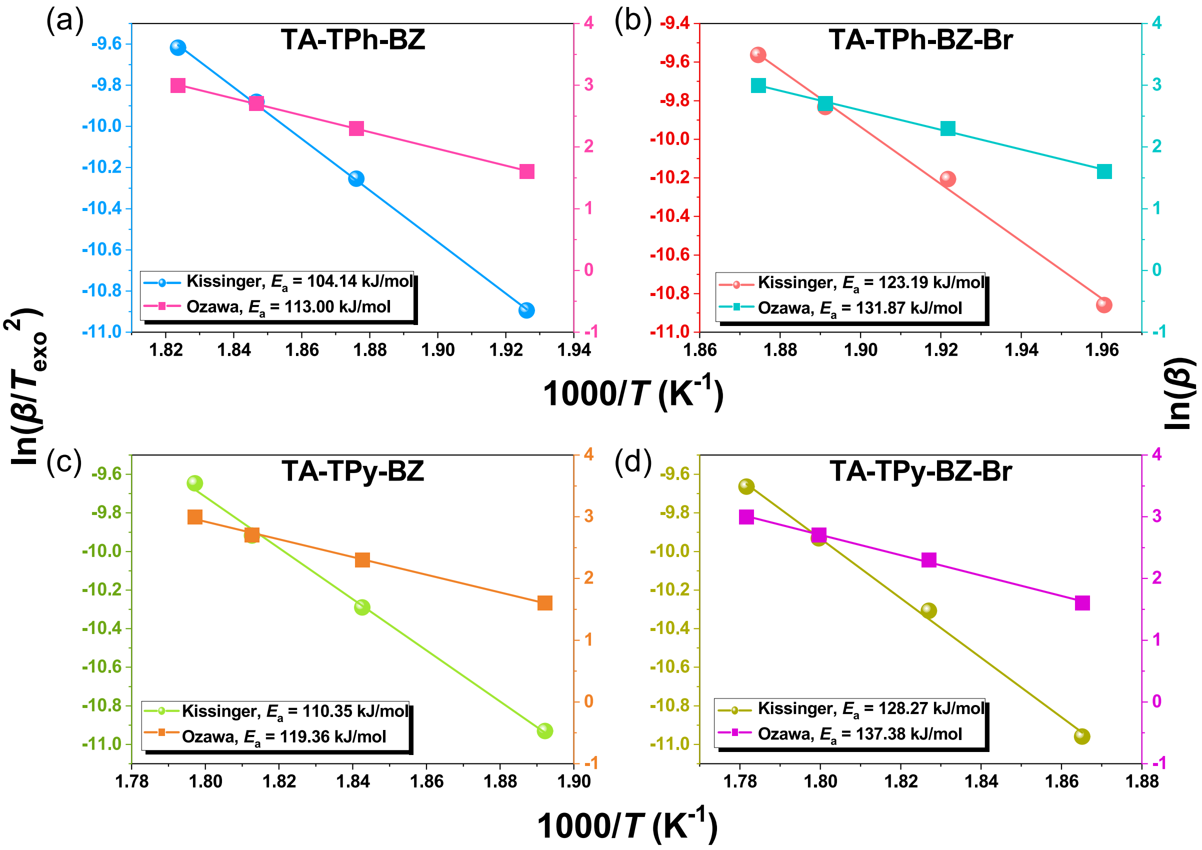

**Figure 5.** Kissinger and Ozawa plots for the estimation of the values of Ea of (a) TA-TPh-BZ, (b) TA-TPh-BZ-Br, (c) TA-TPy-BZ, and (d) TA-TPy-BZ-Br.

influences hydrogen bond interactions and that the structure involving the Ar−**CH$_2$**−N moiety and pyridine is more stable. Figure S23a-d present reduced density gradient (RDG) plots for the triazine-based Schiff base monomers TA-TPh-SF, TA-TPy-SF, TA-TPh-BZ, and TA-TPy-BZ. RDG plots are effective for visualizing noncovalent interactions. In these plots, monomers containing a benzene ring exhibit primarily Van Der Waals interactions (indicated by green regions), whereas those with pyridine moieties display both hydrogen bonding (shown as blue surfaces) and Van Der Waals forces. Notably, only TA-TPy-SF adopts a completely planar configuration, indicating that the protons on its imine bond and phenolic groups are strongly influenced by an aromatic ring current effect. In contrast, TA-TPh-SF, TA-TPh-BZ, and TA-TPy-BZ demonstrate nonplanar structures. Interestingly, the structure of TA-TPy-BZ exhibits a more planar configuration than TA-TPh-BZ, which indicates the presence of intramolecular hydrogen bonding between the oxazine ring and the pyridine moiety. In our density functional theory (DFT) calculations, Figure S24 displays the HOMO and LUMO distributions for TA-TPh-SF and TA-TPh-SF-Br. In both molecules, the LUMO is delocalized over the entire system, whereas the HOMO shows only a minor contribution from the triazine ring. The HOMO−LUMO energy gaps are 3.71 eV for TA-TPh-SF and 3.72 eV for TA-TPh-SF-Br, which are values that are lower than those observed in the TA-TPh-BZ. Similarly, TA-TPy-SF and TA-TPy-SF-Br present HOMO and LUMO distributions similar to the TPh series; nonetheless, their orbital energies are lower, rendering them more stable. Furthermore, these Schiff base monomers have a HOMO−LUMO gap that is approximately 0.2 eV smaller, indicating increased chemical reactivity, which is further enhanced by their planar geometry that improves conjugation.

Figure 4 illustrates that TA-TPh-BZ has a HOMO−LUMO gap of 4.10 eV, with the LUMO delocalized throughout the conjugated system and the HOMO concentrated in both the conjugated system and the oxazine ring. In TA-TPh-BZ-Br, bromine incorporation shifts the LUMO energy from −2.05 to −2.13 eV and the HOMO energy from −6.15 to −6.28 eV, slightly increasing the gap to 4.15 eV. Similarly, in TA-TPy-BZ, the LUMO is localized within the conjugated system while the HOMO extends over both the conjugated system and the oxazine ring, resulting in a gap of 4.15 eV; the addition of bromine increases this gap marginally to 4.19 eV. Furthermore, these benzoxazine monomers exhibit a HOMO−LUMO gap that is approximately 0.05 eV higher, indicating decreased chemical reactivity, a trend that is also reflected in the dynamic DSC heat release curves [Figure S27].

Molecular electrostatic potential (MESP) maps highlight the electrophilic and nucleophilic regions of a molecule, with red areas indicating regions of high electron density (more negative ESP), and blue areas denoting electron-deficient regions (more positive ESP). In the triazine-based Schiff base monomers, the nitrogen atom in the triazine ring is the most nucleophilic site, with ESP values ranging from −27 to −30 kcal/mol, followed by the hydroxyl oxygen, which exhibits ESP values between −25 and −28 kcal/mol. These observations, along with the effect of bromine substitution, are confirmed in Figure S25a-d. In the TA-TPh-BZ, Figure S26a-d show that the nitrogen atom in the triazine ring has the most negative potential at −32 kcal/mol, while the terminal hydrogen reveals the most positive potential at +23 kcal/mol. In TA-TPh-BZ-Br, a similar trend is observed; however, the incorporation of a bromine atom slightly reduces the negative ESP values and increases the positive ones ascribed to the electron-withdrawing effect of the bromine atom. Similarly, in TA-TPy-BZ, the triazine nitrogen reveals the highest negative ESP at −31 kcal/mol, with the terminal hydrogen showing a positive potential of +27 kcal/mol. For TA-TPy-BZ-Br, the same trend applies; the addition of bromine leads to a slight alteration in these values.

Figure S27a-d manifest DSC profiles of the four triazine-based benzoxazine monomers recorded at various heating rates, which were employed to investigate their polymerization kinetics. As the heating rate diminished, both the $T_m$ and the ROP peaks shifted to lower temperatures. Notably, the benzoxazine monomers containing a bromine substituent demonstrated a much smaller shift in the ROP peaks across different heating rates. This behavior is attributed to variations in the interactions between the oxazine ring and adjacent aromatic groups (either benzene or pyridine moieties), which in turn alter the activation energy ($E_a$) required for the polymerization process. The values of $E_a$ were determined using both the Kissinger and Ozawa methods. Figure 5a-d unveils the corresponding plots of ln ($\beta/T_{exo}{}^2$ and ln ($\beta$) versus $1/T_{exo}$. The calculated activation energy values are 104.14 (Kissinger) and 113.00 kJ/mol (Ozawa) for TA-TPh-BZ, 123.19 (Kissinger) and 131.87 kJ/mol (Ozawa) for TA-TPh-BZ-Br, 110.35 (Kissinger) and 119.36 kJ/mol for TA-TPy-BZ, and 128.27 (Kissinger) and 137.38 kJ/mol (Ozawa) for TA-TPy-BZ-Br, respectively [Table 1]. These results highlight the influence of bromine substitution and hydrogen-bonding interactions on the polymerization kinetics of these benzoxazines.

The XRD analysis of the thermally treated triazine-based benzoxazines at 280 °C reveals distinct differences in local chain packing among the samples in Figure S28. Poly(TA-TPh-BZ) reveals the highest halo intensity, indicating the greatest degree of short-range ordering. This enhanced packing can be attributed to the planar benzene structure of the monomer and the predominance of Van Der Waals and $\pi$-$\pi$ interactions between benzene rings, which facilitate uniform chain alignment. In contrast, poly(TA-TPh-BZ-Br) displays slightly reduced intensity, as the introduction of a bromine atom introduces steric hindrance and an electron-withdrawing effect that mildly disrupts chain packing. Further reductions in halo intensity are observed in the TPy series. Both poly(TA-TPy-BZ) and poly(TA-TPy-BZ-Br) exhibit significantly lower intensities, reflecting decreased local ordering. This can be ascribed to the formation of strong intramolecular hydrogen bonds between the pyridine and oxazine units, which enforce a rigid and planar molecular geometry. Although this conformation enhances conjugation, it also restricts interchain flexibility and diminishes the ability of adjacent chains to align and stack efficiently. The increased polarity and directional nature of these hydrogen bonds further inhibit effective packing. These observations suggest a strong correlation between hydrogen-bonding interactions and local structural organization. Specifically, the presence of intramolecular hydrogen bonds and bromine substitution diminishes short-range order, as evidenced by weaker amorphous halos. In contrast, systems dominated by nondirectional van der Waals interactions, such as the TPh-based polymers, achieve more efficient packing, resulting in stronger halo intensity in the XRD patterns.[64,65] Table S9 summarizes the characteristics of the synthesized triazine-based benzoxazine monomers. All BZ monomers investigated in this study demonstrated excellent thermal stability. Notably, the triazine-based BZ monomers containing bromine are particularly promising for the fabrication of porous materials applicable to gas capture, dye adsorption, and metal ion sensing.

## ■ CONCLUSIONS

We successfully synthesized and characterized two series of triazine-based benzoxazine monomers using both aniline and aminopyridine derivatives. Detailed spectroscopic analyses confirmed the formation of key intermediates and final products through well-defined reaction pathways. Our NMR data, RDG plots, and DFT studies revealed that intramolecular hydrogen bonding and aromatic ring current effects play crucial roles in determining the electronic and structural properties of these monomers, with the pyridine-based systems evincing unique planar configurations and enhanced conjugation. Bromine substitution was shown to further modulate the electronic properties by slightly increasing the HOMO−LUMO gaps and influencing the polymerization kinetics, as corroborated by DSC and activation energy analyses. These findings not only enhance our understanding of structure−property relationships in benzoxazine systems but also highlight the potential of these materials for high-performance applications in adhesive, coating, electronics, aerospace, and beyond. In addition, brominated triazine-based benzoxazine monomers show great promise as precursors for porous materials used in gas capture, dye adsorption, and metal ion sensing.

## ■ ASSOCIATED CONTENT

### Supporting Information

The Supporting Information is available free of charge at https://pubs.acs.org/doi/10.1021/acsapm.5c02017.

> Characterization, synthesis; FTIR and NMR spectroscopy of synthesized intermediates and benzoxazine monomers; ESI-MS, elemental analyses; the possible molecular structure of TA-TPh-BZ, TA-TPh-BZ-Br, TA-TPy-BZ, and TA-TPy-BZ-Br after ROP reaction; TGA profiles of TA-TPh-BZ, TA-TPh-BZ-Br, TA-TPy-BZ, and TA-TPy-BZ-Br; dynamic FTIR and DSC profiles of TA-TPh-BZ, TA-TPh-BZ-Br, TA-TPy-BZ, and TA-TPy-BZ-Br; the HOMO and LUMO isosurface maps electrostatic potential (ESP) distributions of TA-TPh-SF, TA-TPh-SF-Br, TA-TPy-SF, and TA-TPh-SF-Br; XRD spectra of poly(triazine-based benzoxazine) after thermal treatment at 280 °C (PDF)

## ■ AUTHOR INFORMATION

### Corresponding Author

**Shiao-Wei Kuo** − *Department of Materials and Optoelectronic Science, Center of Crystal Research, National Sun Yat-Sen University, Kaohsiung 804, Taiwan; Department of Medicinal and Applied Chemistry, Kaohsiung Medical University, Kaohsiung 807, Taiwan;* orcid.org/0000-0002-4306-7171; Email: kuosw@faculty.nsysu.edu.tw

## Authors

**Yang-Chin Kao** − *Department of Materials and Optoelectronic Science, Center of Crystal Research, National Sun Yat-Sen University, Kaohsiung 804, Taiwan*

**Mohamed Gamal Mohamed** − *Department of Materials and Optoelectronic Science, Center of Crystal Research, National Sun Yat-Sen University, Kaohsiung 804, Taiwan; Chemistry Department, Faculty of Science, Assiut University, Assiut 71515, Egypt*; orcid.org/0000-0003-0301-8372

**Pin-Han Chen** − *Department of Materials and Optoelectronic Science, Center of Crystal Research, National Sun Yat-Sen University, Kaohsiung 804, Taiwan*

**Alaa Ali Thabet** − *Chemistry Department, Faculty of Science, Assiut University, Assiut 71515, Egypt*

**Ahmed A. K. Mohammed** − *Chemistry Department, Faculty of Science, Assiut University, Assiut 71515, Egypt*

Complete contact information is available at: https://pubs.acs.org/10.1021/acsapm.5c02017

## Author Contributions

[‖]Y.-C.K. and M.G.M. contributed equally.

## Notes

The authors declare no competing financial interest.

## ACKNOWLEDGMENTS

This study was supported financially by the National Science and Technology Council, Taiwan, under contracts NSTC 113-2223-E-110-001- and 113-2221-E-110-012-MY3.

## REFERENCES

(1) Yang, R.; Zhang, K. Design and Synthesis of Flavonoid-Based Mono-, Bis-, and Tri-Benzoxazines: Toward Elucidating Roles of Oxazine Ring Number and Hydrogen Bonding on Their Polymerization Mechanisms and Thermal Properties. *Macromolecules* **2025**, *58*, 616−626.

(2) Mukherjee, S.; Lochab, B. Hydrogen bonding-guided strategies for thermal performance modulation in biobased oxazine ring-substituted benzoxazine thermosets. *Macromolecules* **2024**, *57*, 1795−1807.

(3) Mohamed, M. G.; Li, C. J.; Khan, M. A. R.; Liaw, C. C.; Zhang, K.; Kuo, S. W. Formaldehyde-Free Synthesis of Fully Bio-Based Multifunctional Bisbenzoxazine Resins from Natural Renewable Starting Materials. *Macromolecules* **2022**, *55* (8), 3106−3115.

(4) Zeng, M.; Luo, H.; Feng, Z.; He, N.; Tang, C.; Chen, J.; Zeng, D.; Zhou, Y.; Shen, Y. Structural design and polymerization of High-Frequency low dielectric benzoxazine resins. *ACS Appl. Polym. Mater.* **2024**, *6*, 6614−6626.

(5) Appasamy, S.; Krishnasamy, B.; Guruselvalakshmi, M.; Ramachandran, S.; Muthukaruppan, A. Vanillin derived partially bio-based benzoxazine resins for hydrophobic coating and anti-corrosion applications: Studies on syntheses and thermal behavior. *Polym. -Plast. Technol. Mater.* **2023**, *63* (3), 287−298.

(6) Suesuwan, A.; Suetrong, N.; Yaemphutchong, S.; Tiewlamsam, I.; Chansaenpak, K.; Wannapaiboon, S.; Chuanopparat, N.; Srathongsian, L.; Kanjanaboos, P.; Chanthaset, N.; Wattanathana, W. Partially Bio-Based Benzoxazine Monomers Derived from Thymol: Photoluminescent Properties, Polymerization Characteristics, Hydrophobic Coating Investigations, and Anticorrosion Studies. *Polymers* **2024**, *16*, 1767.

(7) Lu, Y.; Liu, J.; Zhao, W.; Zhang, K. Bio-benzoxazine structural design strategy toward highly thermally stable and intrinsically flame-retardant thermosets. *J. Chem. Eng.* **2023**, *457*, 141232.

(8) Akkus, B.; Zhu, H.; Mitsuishi, M. Bio-Based Benzoxazine-Containing Polycyclosiloxanes as Flame-Retardant Adhesive Materials. *ACS Appl. Polym. Mater.* **2024**, *6*, 9466−9476.

(9) Kao, Y. C.; Ku, Y. H.; Mohamed, M. G.; Su, W. H.; Kuo, S. W. Microphase Separation Transformation in Bio-Based Benzoxazine/Phenolic/PEO-*b*-PCL Diblock Copolymer Mixtures Induced by Transesterification Reaction. *Macromolecules* **2025**, *58*, 585−600.

(10) Mohamed, M. G.; Chen, T. C.; Kuo, S. W. Solid-state chemical transformations to enhance gas capture in benzoxazine-linked conjugated microporous polymers. *Macromolecules* **2021**, *54*, 5866−5877.

(11) Sharma, P.; Hakkarainen, M. Light responsive chemistry−A design strategy for remodelling benzoxazine architectures towards room temperature processing. *Mater. Today Chem.* **2024**, *38*, 102073.

(12) Ejaz, M.; Mohamed, M. G.; Kuo, S. W. Fluorescent benzoxazine−perylene linked covalent organic polymer as a sensing probe for lead ions and 2, 4, 6-trinitrophenol. *ACS Appl. Polym. Mater.* **2024**, *6*, 9170−9179.

(13) Mohamed, M. G.; Chen, C. C.; Kuo, S. W. Nitrogen and sulfur co-doped microporous carbon through benzo [c]-1, 2, 5-thiadiazole-functionalized benzoxazine-linkage porous organic polymer in $CO_2$ capture and energy storage. *React. Funct. Polym.* **2025**, *214*, 106286.

(14) Ejaz, M.; Mohamed, M. G.; Chen, Y. T.; Zhang, K.; Kuo, S. W. Porous carbon materials augmented with heteroatoms derived from hyperbranched biobased benzoxazine resins for enhanced $CO_2$ adsorption and exceptional supercapacitor performance. *J. Energy Storage* **2024**, *78*, 110166.

(15) Mohamed, M. G.; Su, B. X.; Kuo, S. W. Robust nitrogen-doped microporous carbon via crown ether-functionalized benzoxazine-linked porous organic polymers for enhanced $CO_2$ adsorption and supercapacitor applications. *ACS Appl. Mater. Interfaces* **2024**, *16*, 40858−40872.

(16) Gulyuz, S.; Kiskan, B. Combination of polyethylenimine and vanillin-based benzoxazine as a straightforward self-healable system with excellent film-forming ability. *Macromolecules* **2024**, *57*, 2078−2089.

(17) Yang, R.; Yang, R.; Yang, S.; Zhang, K. Hydrogen Bonding-Rich Bio-Benzoxazine Resin Provides High-Performance Thermosets and Ultrahigh-Performance Composites. *ACS Sustainable Chem. Eng.* **2024**, *12*, 1728−1739.

(18) Sahu, S.; Lochab, B. Sustainable benzoxazine-sulfur copolymer with dynamic linkages: recycling, reprocessing, self-healing, and shape recovery ($R^2S^2$). *ACS Sustainable Chem. Eng.* **2024**, *12*, 7126−7135.

(19) Malekkhouyan, R.; Van Renterghem, L.; Bonnaud, L.; Paint, Y.; Gonon, M.; Cornil, D.; Cornil, J.; Raquez, J. M.; Olivier, M. G. Effect of surface pretreatment on the production of LDH for post-treatment with benzoxazine resin. *Surf. Coat. Technol.* **2024**, *479*, 130538.

(20) Ribeiro, F. W.; Omari, I.; Scott mcindoe, J.; Correra, T. C. Protonation Effects on the Benzoxazine Formation Pathways and Products Distribution. *ChemPhyschem* **2024**, *25*, No. e202400295.

(21) Liu, Y.; Yuan, L.; Liang, G.; Gu, A. Preparation of thermally resistant and mechanically strong biomass benzoxazine resins via green strategy. *ACS Sustainable Chem. Eng.* **2024**, *12*, 1247−1254.

(22) Hu, C.; Yao, Z.; Zhao, W.; Zhang, K. Synthesis, Characterization, and Structure−Property Investigations of Benzoxazine Resins with Low Surface Free Energy. *Macromol. Chem. Phys.* **2025**, *226*, 2400152.

(23) Mohamed, M. G.; Kuo, S. W. Crown Ether-Functionalized Polybenzoxazine for Metal Ion Adsorption. *Macromolecules* **2020**, *53*, 2420−2429.

(24) Qi, L.; Hu, L. X.; Wang, Z. C.; Yuan, Z. G.; Wen, H. L.; Liu, W. B.; Wang, J.; Derradji, M. Bio-based benzoxazine-terminated hyperbranched polyesters. *React. Funct. Polym.* **2024**, *199*, 105888.

(25) Bessa, W.; Trache, D.; Ghalmi, C.; Aidi, S.; Tarchoun, A. F.; Gahfif, F.; Abdelaziz, A.; Thakur, S.; Hussin, M. H. Curing kinetics of composites based on benzoxazine resin and microcrystalline cellulose modified by phosphorus salt. *Thermochim. Acta* **2024**, *735*, 179718.

(26) Zhao, S.; Zhou, C.; Xin, Z. Effect of the Oxazine Structure on Antibacterial Activity of Biobased Benzoxazine and Its Application in Polyethylene Modification. *ACS Appl. Polym. Mater.* **2025**, *7*, 2879−2889.

(27) Yang, Y.; Lu, Y.; Zhang, K. Improving comprehensive performance of norbornene-furan functionalized benzoxazine resins by regulating the bridge length. *J. Appl. Polym. Sci.* **2024**, *141*, No. e55920.

(28) Kao, Y. C.; Mohamed, M. G.; Chiang, C. H.; Kuo, S. W. Design and Construction of Furan-Based and Thiophene-Based Salicyladazine Bisbenzoxazine Resins with High Thermal Stability and Tunable Surface Properties. *Macromol. Chem. Phys.* **2025**, *226*, 2400091.

(29) Ejaz, M.; Mohamed, M. G.; Huang, W. C.; Kao, Y. C.; Chen, W. C.; Kuo, S. W. Highly thermally stable polyhedral oligomeric silsesquioxane based on diacetal-functionalized polybenzoxazine nanocomposites. *Eur. Polym.J* **2025**, *223*, 113649.

(30) Hsiao, C.-W.; Mohamed, M. G.; Kuo, S.-W. Structural design and functionalization of benzoxazine-modified octavinylsilsesquioxane hybrid porous polymer through Sonogashira coupling reaction. *Mater. Today Chem.* **2025**, *46*, 1027955.

(31) Yuan, M.; Lu, X.; Kuo, S. W.; Xin, Z. Structure−Performance Relationship of Low-*k* Polybenzoxazine Based on Molecular Simulation. *ACS Appl. Polym. Mater.* **2024**, *6*, 4195−4203.

(32) Yuan, X.; Su, X.; Wang, Y.; Liu, L.; Li, R.; Wang, C. Benzoxazine monomers with antibacterial property and polybenzoxazines for preventing adhesion to bacteria. *ACS Appl. Polym. Mater.* **2023**, *5* (7), 5650−5661.

(33) Lu, Y.; Li, N.; Peng, Y.; Mohamed, M. G.; Kuo, S. W.; Zhang, K. Facile and eco-friendly synthesis of hydrogen bonding-rich bio-based bisbenzoxazine resins with low surface free energy, strong adhesion strength and high thermal stability. *Mol. Syst. Des. Eng.* **2024**, *9*, 86−98.

(34) Mohamed, M. G.; Chen, C.-C.; Zhang, K.; Kuo, S.-W. Construction of three-dimensional porous organic polymers with enhanced $CO_2$ uptake performance via solid-state thermal conversion from tetrahedral benzoxazine-linked precursor. *Eur. Polym. J.* **2023**, *200*, 112551.

(35) Ejaz, M.; Mohamed, M. G.; Kuo, S. W. Solid state chemical transformation provides a fully benzoxazine-linked porous organic polymer displaying enhanced $CO_2$ capture and supercapacitor performance. *Polym. Chem.* **2023**, *14*, 2494−2509.

(36) Mohamed, M. G.; Chang, W. C.; Kuo, S. W. Crown ether-and benzoxazine-linked porous organic polymers displaying enhanced metal ion and $CO_2$ capture through solid-state chemical transformation. *Macromolecules* **2022**, *55*, 7879−7892.

(37) Ejaz, M.; Mohamed, M. G.; Kuo, S. W. Benzoxazine-Linked Polyhedral Oligomeric Silsesquioxane: 3D Porous Organic-Inorganic Polymer for Improved $CO_2$ Capture and Supercapacitor Performance. *J. Taiwan Inst. Chem. Eng.* **2025**, *2025*, 106098.

(38) Liu, M.; Guo, L.; Jin, S.; Tan, B. Covalent triazine frameworks: synthesis and applications. *J. Mater. Chem. A* **2019**, *7*, 5153−5172.

(39) Maliszewski, D.; Drozdowska, D. Recent advances in the biological activity of *s*-triazine core compounds. *Pharmaceuticals* **2022**, *15*, 221.

(40) Krishnaraj, C.; Jena, H. S.; Leus, K.; Van Der Voort, P. Covalent triazine frameworks−a sustainable perspective. *Green Chem.* **2020**, *22*, 1038−1071.

(41) Qian, Z.; Wang, Z. J.; Zhang, K. A. Covalent triazine frameworks as emerging heterogeneous photocatalysts. *Chem. Mater.* **2021**, *33*, 1909−1926.

(42) Liao, L.; Li, M.; Yin, Y.; Chen, J.; Zhong, Q.; Du, R.; Liu, S.; He, Y.; Fu, W.; Zeng, F. Advances in the synthesis of covalent triazine frameworks. *ACS Omega* **2023**, *8*, 4527−4542.

(43) Xiong, P.; Zhang, S.; Wang, R.; Zhang, L.; Ma, Q.; Ren, X.; Gao, Y.; Wang, Z.; Guo, Z.; Zhang, C. Covalent triazine frameworks for advanced energy storage: challenges and new opportunities. *Energy Environ. Sci.* **2023**, *16*, 3181−3213.

(44) Cerón, V. D.; Illicachi, L. A.; Insuasty, B. Triazine: an important building block of organic materials for solar cell application. *Molecules* **2023**, *28* (1), 257.

(45) Zhang, F. G.; Chen, Z.; Tang, X.; Ma, J. A. Triazines: syntheses and inverse electron-demand Diels−Alder reactions. *Chem. Rev.* **2021**, *121*, 14555−14593.

(46) Aggarwal, S.; Awasthi, S. K. Emerging trends in the development and applications of triazine-based covalent organic polymers: a comprehensive review. *Dalton Trans.* **2024**, *53*, 11601−11643.

(47) Chu, Y.; Zhao, F.; Meng, F.; Zhang, W.; Zhao, J.; Zhong, X. Donor-acceptor type conjugated porous polymers based on benzotrithiophen and triazine derivatives: Effect of linkage unit on photocatalytic water splitting. *Int. J. Hydrogen Energy* **2024**, *64*, 109−119.

(48) Sathiyan, G.; Venkatesan, G.; Ramasamy, S. K.; Lee, J.; Barathi, S. Recent progress in triazine-based fluorescent probes for detecting hazardous nitroaromatic compounds. *J. Environ. Chem. Eng.* **2024**, *12*, 112804.

(49) Kumar, N. R.; Agrawal, A. R. Advances in the Chemistry of 2,4,6-Tri (thiophen-2-yl)-1, 3, 5-triazine. *ChemistryOpen* **2023**, *12* (1), No. e202200203.

(50) Barakat, A.; El-Faham, A.; Haukka, M.; Al-Majid, A. M.; Soliman, S. M. *s*-Triazine pincer ligands: Synthesis of their metal complexes, coordination behavior, and applications. *Appl. Organomet. Chem.* **2021**, *35*, No. e6317.

(51) Audebert, P.; Kroke, E.; Posern, C.; Lee, S. H. State of the art in the preparation and properties of molecular monomeric *s*-heptazines: Syntheses, characteristics, and functional applications. *Chem. Rev.* **2021**, *121*, 2515−2544.

(52) Alshubramy, M. A.; Alamry, K. A.; Hussein, M. A. An overview of the synthetic strategies of C 3-symmetric polymeric materials containing benzene and triazine cores and their biomedical applications. *RSC Adv.* **2023**, *13*, 14317−14339.

(53) Sahu, D.; Sreekanth, P. R.; Behera, P. K.; Pradhan, M. K.; Patnaik, A.; Salunkhe, S.; Cep, R. Advances in synthesis, medicinal properties and biomedical applications of pyridine derivatives: A comprehensive review. *Eur. J. Med. Chem. Rep.* **2024**, *12*, 100210.

(54) Zakharychev, V. V.; Martsynkevich, A. M. Development of novel pyridine-based agrochemicals: a review. *Adv. Agrochem* **2025**, *4* (1), 30−48.

(55) Kawaguchi, A. W.; Sudo, A.; Endo, T. Functional 1, 3-benzoxazine bearing 4-pyridyl group: Synthesis and thermally induced polymerization behavior. *J. Polym. Sci.; Part A: Polym. Chem.* **2014**, *52*, 410−416.

(56) Fan, X.; Li, S.; Wang, C.; Deng, Y.; Zhang, C.; Wang, Z. Research on fluoropyridine-based benzoxazine with high thermal stability and excellent flame retardancy for its application in coatings. *Eur. Polym. J.* **2023**, *187*, 111884.

(57) Shibayama, Y.; Kawauchi, T.; Takeichi, T. Synthesis and properties of polybenzoxazines containing pyridyl group. *High Perform. Polym.* **2014**, *26*, 60−68.

(58) Lin, C. H.; Shih, Y. S.; Wang, M. W.; Tseng, C. Y.; Juang, T. Y.; Wang, C. F. Emission and surface properties of main-chain type polybenzoxazine with pyridinyl moieties. *RSC Adv.* **2014**, *4*, 8692−8698.

(59) Mohamed, M. G.; Su, W. C.; Lin, Y. C.; Wang, C. F.; Chen, J. K.; Jeong, K. U.; Kuo, S. W. Azopyridine-functionalized benzoxazine with $Zn(ClO_4)_2$ form high-performance polybenzoxazine stabilized through metal−ligand coordination. *RSC Adv.* **2014**, *4*, 50373−50385.

(60) Albert, A.; Goldacre, R.; Phillips, J. The strength of heterocyclic bases. *J. Chem. Soc.* **1948**, *1948*, 2240−2249.

(61) Lakshmanan, K.; Angayarkanny, S. Synthesis and Characterization of Bio-Based Benzoxazine Monomer for Metal Sensing Applications and to Form Fire-Retardant Polymer. *J. Appl. Polym. Sci.* **2025**, *142*, No. e57232.

(62) Mydeen, K. M.; Krishnasamy, B. Sustainable benzoxazine materials from renewable sources: Synthesis, corrosion resistance, dielectric and superhydrophobic studies. *Eur. Polym. J.* **2025**, *234*, 114017.

(63) Emamian, S.; Lu, T.; Kruse, H.; Emamian, H. Exploring nature and predicting strength of hydrogen bonds: a correlation analysis between atoms-in-molecules descriptors, binding energies, and energy

components of symmetry-adapted perturbation theory. *J. Comput. Chem.* **2019**, *40*, 2868−2881.

(64) Liu, Y.; Li, J.; Cai, J.; Zhang, X.; Hu, L.; Pang, S.; He, C. Intramolecular hydrogen bonds assisted construction of planar tricyclic structures for insensitive and highly thermostable energetic materials. *Int. J. Mol. Sci.* **2024**, *25*, 3910.

(65) Zhang, J.; Li, X. Intramolecular hydrogen bonding, π-π stacking interactions, and substituent effects of 8-hydroxyquinoline derivative supermolecular structures: A theoretical study. *J. Mol. Model.* **2019**, *25*, 241.